Bio-inspired vortex lift for enhanced manoeuvrability

A. Domínguez[1], J. Tomé[2], E. Gowree[3] and M. Bauerheim[4]

[1]*ISAE-SUPAERO, 31400, France*

[2]*ISAE-SUPAERO, 31400, France*

[2]*ISAE-SUPAERO, 31400, France, erwin-ricky.gowree@isae-supaero.fr*

[2]*ISAE-SUPAERO, 31400, France, michael.bauerheim@isae-supaero.fr*

ABSTRACT

Inspired by highly manoeuvrable species of birds like the peregrine falcon and the swift, static and dynamic computational fluid dynamics (CFD) simulations were conducted to investigate vortex lift in unsteady flows. The configuration corresponds to a $50°$ sweep delta wing with sharp leading edge at Re= 5.0×10^4. CFD simulations were performed using a Direct Numerical Simulation (DNS) approach with a Lattice-Boltzmann Method as well as Unsteady Reynolds Averaged Navier-Stokes (URANS) simulations. Aerodynamic forces as well as the overall structure of the leading edge vortices were compared with existing literature. The evolution of the flow structures was studied when the wing performs a pitching manoeuvre from $0°$ to $20°$ angle of attack. Close agreement between both methods was found for the static and pitching lift curves, with the URANS solver presenting substantial limitations to capture complex unsteady phenomena such as the vortex breakdown. A time lag was observed in the flow dynamics during the manoeuvre, with the vortex breakdown delayed during pitch-up resulting in an improved aerodynamics performance, but more present and intense when pitching down. A sinusoidal motion was tested with the URANS solver and compared with the linear ramp case, showing performance advantages as well as higher similarity to real manoeuvres.

1. INTRODUCTION

Birds, such as the peregrine falcon and the swift, are known for their high manoeuvrability, associated with their morphological transformation capability during flight [6]. In particular, the peregrine falcon wing's sweep angle (Λ) can vary from $\Lambda_{min} = 40°$ (fig. 1) to ap-

proximately $90°$, which allows them to adapt to different flight phases, being able to increase their maximum speed or pull out from a dive.
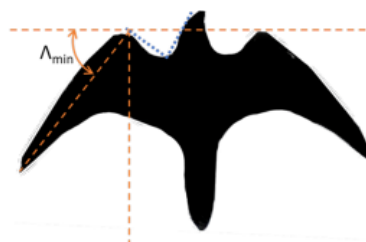

Figure 1: Wing shape adopted by the falcon during the final phase of the pull-out manoeuvre [8]

Previous experimental and high-fidelity simulations by Gowree et al. [3] showed that the flow over a peregrine falcon was dominated by large vortical structures. In their subsequent study [8] they demonstrated that in fact the overall lift force of the peregrine falcon's wings agrees well with the delta wing lift theory, which suggests the similitude between these two configurations.

Delta wings exhibit a leading-edge vortex (LEV) at low Reynolds number, even at low incidence [4]. Due to the LEV, these planforms reach higher stall angles while generating higher lift than conventional wings, thus enhancing manoeuvrability. While extensive research for slender delta wings (typically with a sweep angle greater than $60°$) has been carried out, both numerically and experimentally, considerably less investigation has been undertaken for nonslender wings ($\Lambda < 55°$). Depending on the Reynolds number and incidence, nonslender wings will exhibit a dual or trial vortex structure, contrasting with the less energetic secondary vortex seen on slender configurations. In addition, nonslender delta wings will exhibit early vortex breakdown, which will lead to a de-

crease in lift as well as more intense unsteadiness.

Consequently, the early vortex breakdown and increased unsteadiness, characteristic of nonslender planforms, can affect the manoeuvrability and stability of these wings. Recent numerical and experimental studies by Yi et al. [11] have shown that, for a sinusoidal pitching movement, the unsteady effect becomes dominant with substantial differences when pitching up and pitching down. On one hand, a strong and coherent LEV is found when pitching up, but vortex breakdown is found close to the apex when pitching down even at angles of incidence corresponding to pre-stall on the static case. In addition, lift hysteresis is observed and found to be enhanced by greater reduced frequencies. At high pitch-up rates, the strong LEV and its delayed breakdown phenomenon create a local suction peak, which translates into an increase in lift. On the other hand, when pitching down, the lower surface of the wing becomes a suction surface, resulting in a lift loss when comparing to the static case.

Yavuz [10] investigated the transformation of the flow structure of a $50°$ swept wing undergoing a ramp pitch-up manoeuvre at low Reynolds numbers of 15 000 and 20 000. One of the vortex in the dual vortex system was observed to be absent, as well as the appearance of vortex breakdown at higher angle of incidence. Due to the pitch up movement, a time lag is observed in the development of the flow structures.

The present investigation focuses on the evolution of the force and vortex structures when performing not only a pitch-up, but also a pitch-down manoeuvre, as the results and flow dynamics between both of them will differ substantially, as well as when comparing them to the static case. The scope of this study is to establish a baseline tool which can be further developed towards its application to future bio-inspired MAV's and UAV's, hence the choice of a nonslender planform and low Reynolds number configuration.

2. NUMERICAL METHODOLOGY

The configuration considered consists of a $50°$ sweep non-slender delta wing with sharp leading edge (fig. 2), at a Reynolds number of 5×10^4. Two approaches are employed: (1) Unsteady Reynolds Averaged Navier-Stokes (URANS) simulations using the commercial software *STAR-CCM+*, and (2) Direct Numerical Simulations (DNS) with a low-dispersion Lattice-Boltzmann method (LBM).

Static numerical simulations for angles of attack of $5°$ and $15°$ were performed with LBM, whereas $5°$, $10°$, $15°$ and $20°$ were simulated with the URANS approach. For the pitching movement, a $[0°\text{-}20°\text{-}0°]$ linear ramp pitch-up and pitch-down movement (as shown in fig. 3) was considered, with a constant pitch rate of $\pm10°$/s.
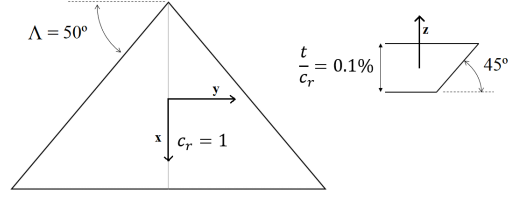

Figure 2: Top view of the geometry (left) and detailed view of the leading edge (right)
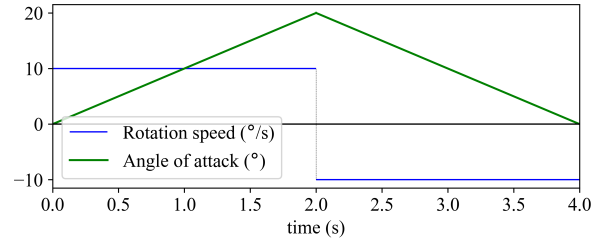

Figure 3: Linear ramp movement

2.1 Lattice-Boltzmann Method

The numerical simulations using the Lattice-Boltzmann method were carried out using the open source code *Palabos* [5]. Rather than focusing on the macroscopic fluid quantities, this low-dispersive method tracks the time and space evolution of a discrete particle distribution function $(F_i(x,t)))$ at a discretized velocity c_i on a lattice grid. The Lattice-Boltzmann advection equation reads:

$$F_i(x+c_i\Delta t, t+\Delta t) - F_i(x,t) = -\frac{1}{\tau}(F_i(x,t) - F_i^{eq}(x,t)) \quad (1)$$

where the right hand side of the previous equation is the collision operator, here approximated by the BGK model. This term drives the particle distribution in relation to the equilibrium state with τ as the relaxation time, associated with the viscosity of the flow ν.

It uses a cartesian mesh with a immersed boundary method that allows to have a static mesh when performing pitch manoeuvres, provided that the geometry stays in the finest grid level. The computational domain was defined as a cube with a side length equal to 40c, and the delta wing was placed in the center.

The cartesian grid contains 7 refinement levels with a total of approximately 95 million cells. The minimum and maximum cell size and time-step considered for the simulations are given in table 1. Time and mesh Independence studies were carried out to ensure correct resolution.

$\Delta x_{min}/c_r$	$\Delta x_{max}/c_r$	$\Delta t \cdot U_0/c_r$
0.003	0.192	1.92×10^4

Table 1: Time and space characteristics of the LBM grid

2.1.1 Grid spacing influence

An initial assessment of the influence of the grid spacing was performed. In the LBM solver, due to the nature of the cartesian grid, the spacing was constant in all three coordinates. The results will be presented in relation to $c/\Delta x$, the number of cells along the chord of the delta wing.
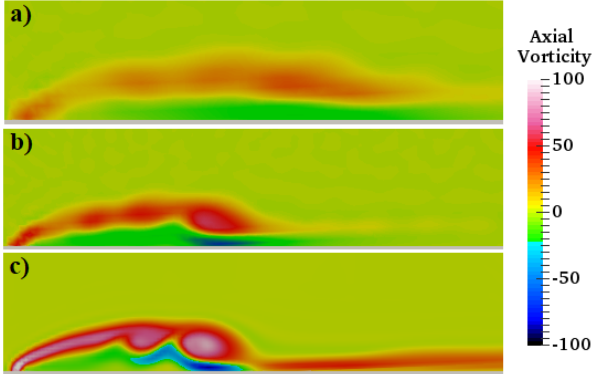

Figure 4: Axial vorticity obtained with LBM, at x/c = 0.5, plotted on a plane perpendicular to the vortex core for 3 different meshes: **a)** – $c_r/\Delta x$ = 154, **b)** – $c_r/\Delta x$ = 205 and **c)** – $c_r/\Delta x$ = 333

.

Figure 4 depicts the axial vorticity for 3 different meshes, plotted on a plane perpendicular to the vortex core. As observed, in the coarser mesh ($c_r/\Delta x$ = 154), the structures do not resemble a classical dual-vortex structure found in these configurations at 5° of angle of attack [2]. In fact, the expected behaviour is only found for the higher resolution ($c_r/\Delta x$ = 333).

2.2 URANS

A set of unsteady RANS simulations in *STAR-CCM+* were conducted in parallel with the LBM counterparts. The main objective is to use the force evolution data and main flow behaviour if validated with the DNS due to the lack of experimental results in the literature. Although it is expected that this approach will lack the resolution of the latter, with difficulties capturing complex unsteady flow dynamics like the vortex breakdown and its evolution during manoeuvres.

The meshing domain consists of a moving region containing the wing geometry and space where the main vortical activity is expected, placed inside an outer static domain. Both meshes interact through an overset interface, where the moving region is contained within the smallest refinement level of the static one throughout the rotating motion. For better consistency and coherence when comparing the results, both static and dynamic simulations have been carried out using this meshing approach, even though for the static case it would not be required.

An unstructured trimmer mesh with no prism layer has been used for the case, as it will consist essentially on a separated flow. The total number of cells is around 8.4 million, with only 1.4 million corresponding to the outer static region and the remaining 7 million to the inner overset mesh.

The outer static domain applies a coarse mesh with 6 levels of refinement and 4 layers per level. The two finest levels have been stretched downstream for a better capturing of the wake, with the cell size of the most refined matching the one at the outer boundaries of the inner overset mesh (figure 5). The moving overset mesh follows the same approach, although with a considerably lower cell size. This region presents 4 refinement levels ranging between 8 and 12 layers each, the finest being located around the sharp leading edge, with a cell size $dx_{min} = 0.488$ mm.
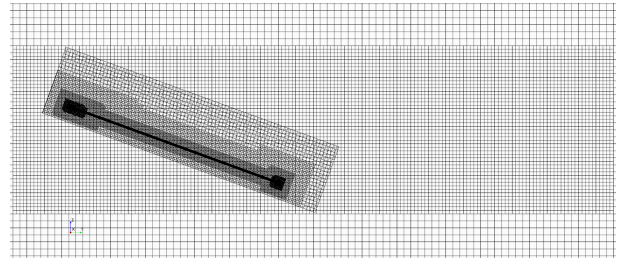

Figure 5: Rotating overset mesh inside most refined level of static domain in the x-z plane. The wing is represented at $\alpha = 20°$.

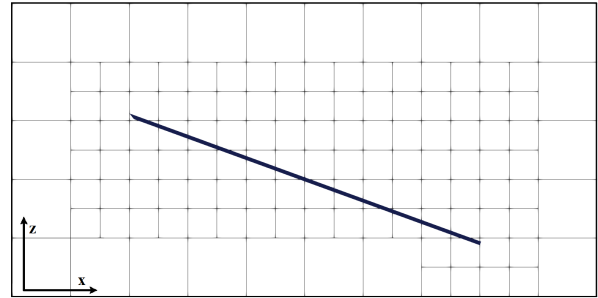
Figure 6: Close-up view of the computational domain in the x-z plane. The delta wing is represented at its maximal angle of attack at $\alpha = 20°$. Only 6 refinement level are represented in this figure.

An extensive mesh independence study has been carried out to arrive to this point, where different domain and refinement shapes, meshing models, growth rates and cell size values have been tested. A time-step of 0.01 s has been used for the implicit unsteady solver of the static simulations, as it has been proven to be sufficient to capture the unsteadiness associated to the large structures captured by the URANS solver. This value was reduced

to 0.005 s for the rotation in the dynamic cases after an initial static convergence, as to increase the number of time-steps per degree of pitch to 20.

A second order scheme in space and time has been chosen, and the turbulence model used is the Shear-Stress-Transport (SST) $k - \omega$, as it provided closer results to both the literature and LBM simulations, while also better capturing the unsteady behaviour of the flow, unlike other tested options like the $k - \varepsilon$ model.

3. RESULTS AND DISCUSSION

3.1 Static simulations

3.1.1 Lift coefficient

Reliable experimental or high fidelity numerical simulation data is scarce in literature for nonslender delta wings, which limited a thorough verification of the results. According to Polhamus [7], using the leading-edge suction analogy, the vortex-lift has a contribution to the total lift which decreases for lower sweep angles. Nevertheless, even for low angles of attack and low Reynolds number, a dual and trial vortex structure is found in these configurations, resulting in a non-negligible contribution to the overall lift which contradicts the basic assumptions of the theory. In addition, a Reynolds dependency has been observed, suggesting that flow reattachment has an influence on stall [4].
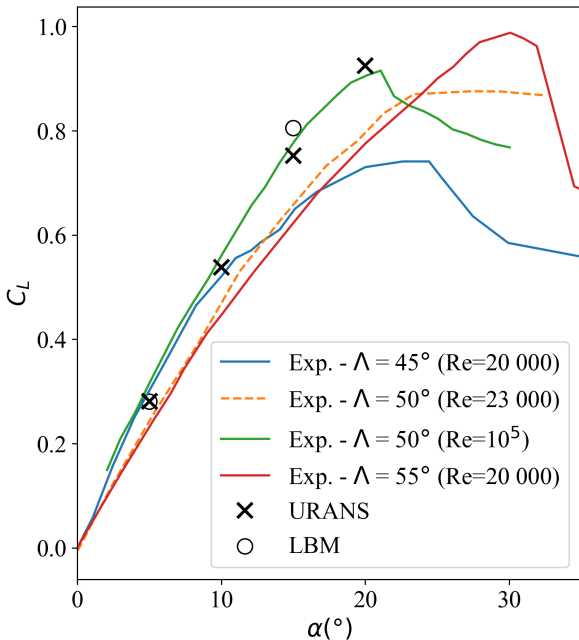

Figure 7: Lift coefficient obtained with URANS and LBM simulations at Re=50 000 compared with experimental results at Re=20 000 and Re=100 000 [1][9][11].

Figure 7 depicts the lift coefficient C_L as a function of the angle of attack α from experimental campaigns conducted at different Reynolds numbers [1][9][11]. By comparing the two experimental curves for $\Lambda = 50°$, one can observe that the maximum lift coefficient $C_{L_{max}}$ increases for smaller Reynolds numbers. However, this also results in a lower α_{max} and a more sudden stall, with a rapid post-stall decrease in C_L. According to Gordnier et al.[2], the increase in Re leads to the strengthening of the dual or trial vortex structure (depending on the incidence), which may lead to higher suction on the surface and therefore higher C_L.

Comparing the curves corresponding to different sweep angles allows to deduce the effect of this parameter on the lift coefficient, where a highly swept delta wing will present increased $C_{L_{max}}$ and α_{max}. However, this will also result in a lower slope and therefore lower C_L at smaller angles of attack, which could influence the planform choice depending on the desired performance when aiming at a potential application.

The results obtained from the URANS and LBM solvers show a good agreement with the experimental data corresponding to the $\Lambda = 50°$, Re=100 000 case [9], even though performed at different Reynolds number. This comparison is justifiable as both Reynolds numbers are outside the sensitive range, presented by Gursul et al. [9] as a region below Re=30 000 where the results are strongly influenced by variations in Re.

3.1.2 Mean flow structure

Figure 8 depicts the axial vorticity at several planes perpendicular to the vortex core. At 5° angle of attack, the vortex structure found using the LBM solver is consistent with the literature.
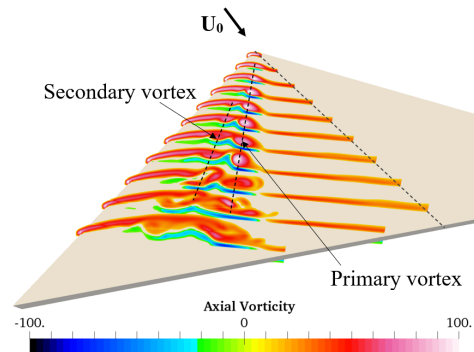

Figure 8: Mean vortex structure over the wing for $\alpha = 5°$

Close to the apex of the wing, a thin shear layer develops, which will later constitute the primary vortex with the greatest intensity. Before reaching half of the chord, the development of a secondary vortex, with the same sign as the primary but less intense, is seen. The existence of this dual vortex structure has been confirmed both numerically and experimentally for nonslender planforms

[4]. The vortex breakdown can be seen in the aft section of the wing, where the loss of coherence of the primary leading-edge vortex is observed, resulting in a highly unsteady behaviour but without causing the wing to stall at this stage.

The streamwise vorticity at two sections along the chord has been plotted for both LBM and URANS approaches (figure 9), in order to compare the capacity to capture the complex flow structures of the latter with the DNS case. Clear differences can be observed for both $x/c = 0.5$ and $x/c = 0.8$ planes. The first one shows a double vortex structure for the LBM case, while only one large primary vortex can be appreciated with URANS. As seen in figure 9a, the vortex breakdown has already occurred at the aft section, however, the flow structures at this angle of attack are not large enough to be captured by the URANS solver, which now shows an averaged double vortex structure with no signs of breakdown.

Figure 10 presents a side-by-side comparison between literature data [2] and one of the static URANS simulations, both corresponding to an angle of attack $\alpha = 15°$. The surface streamlines are plotted over the wing surface, coloured with the pressure coefficient C_p, which allows to observe the relation between the vortical structures the suction they produce over the body. Despite the Reynolds number differing by a factor of 2, both cases are considered as low Re regime, thus it can be observed that the level of agreement with the literature is quite high, with the same vortical structures appearing and similar overall flow behaviour. The primary leading edge vortex can be clearly distinguished, with very close results between both cases in terms of vortex size and angle of the attachment line (PA) with respect to the x-axis. Also, a smaller tertiary vortex can be observed between the primary one and the leading edge of the wing, which breaks down at approximately half of the chord for the Re=26 000 case, and around one third of the chord for the Re=50 000 simulation, suggesting that indeed the vortex breakdown position is affected by the Reynolds number, advancing to-
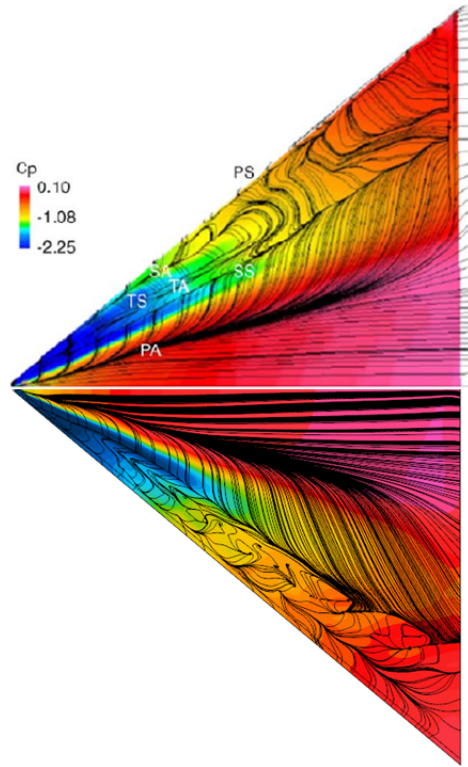
wards the apex as Re increases.

Figure 10: Surface streamline pattern and pressure coefficient at $\alpha = 15°$ from [2] at Re=26 000 (up) and *STAR-CCM+* at Re=50 000 (down).

3.2 Pitch manoeuvre

3.2.1 Evolution of the force

The evolution of the lift coefficient along the manoeuvre, described in section 2, was obtained for both solvers and plotted in figure 11. Due to the sharp discontinuity in the pitch rate at $\alpha = 20°$, the results presented only show
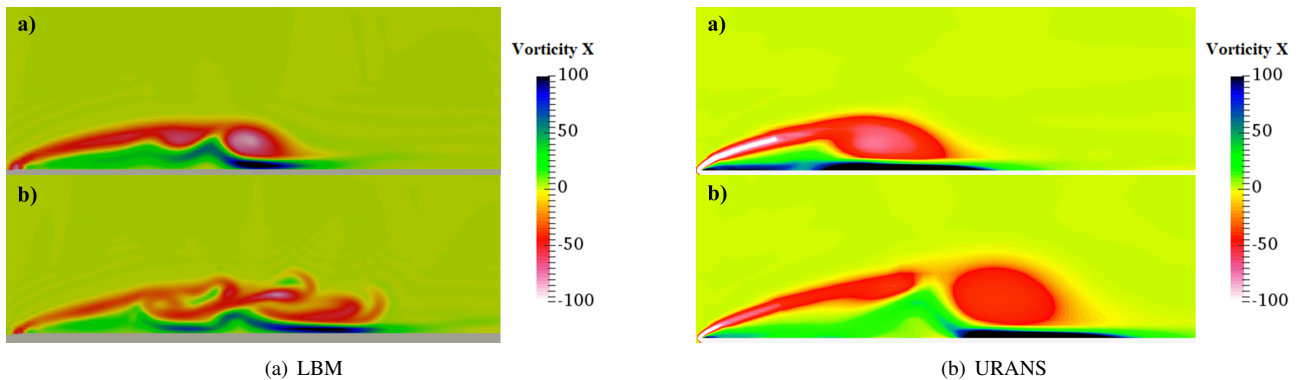
(a) LBM

(b) URANS

Figure 9: Streamwise vorticity with LBM and URANS for $\alpha = 5°$ at axial positions **a)** $x/c = 0.5$ and **b)** $x/c = 0.8$

the lift coefficient for instants after this transition to negative pitch rate. As seen in the figure, there is an excellent agreement between the data obtained from the URANS and LBM solvers.
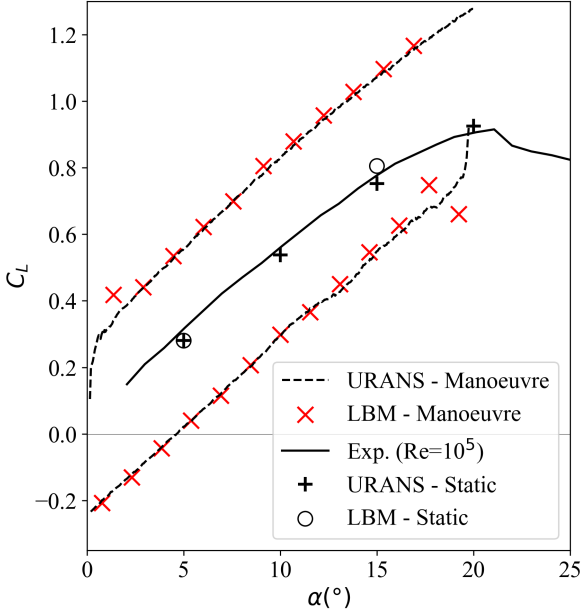

Figure 11: Lift coefficient obtained for the manoeuvre as well as for static experimental and numerical results [9].

Following an initial transient state when initiating the movement, the lift coefficient follows an almost linear trend. In fact, comparing with the static data, the slope of the curve seems to be similar, with a translation $\Delta C_L \approx 0.2$.

When performing a constant pitch up or pitch down manoeuvre, the delta wing sees a change in the effective angle of attack due to the introduction of a vertical velocity component. In this case, denoting Ω [$°/s$] as the pitch rate with axis on the centre of the wing and positive in the y-direction, and α as the angle of attack, the change in local incidence would be of the order of magnitude of $\alpha + 0.5\Omega$. This is consistent with the data found for C_L in figure 11, where the manoeuvre curves at a certain α would match static curves at $\alpha + 5°$ (pitch-up) or $\alpha - 5°$ (pitch-down) for the current case. Nevertheless, a substantially higher value is found for C_L at $\alpha = 20°$ when pitching up ($C_L \approx 1.3$) when comparing to the static case ($C_L \approx 0.9$), suggesting that vortex breakdown and stall are delayed when the wing is manoeuvring. This will be explained in the following section, while analysing the evolution of the vortical structures.

An extra step has been taken following the previous linear ramp manoeuvre, replacing the constant pitch rate by a sinusoidal movement. This could not only ease the simulation convergence at the transition between phases of the manoeuvre, but also improve the performance of the rotating wing. To make the comparison between both approaches possible, the frequency of the movement f=0.25 Hz has been chosen to provide the same average pitch rate along the manoeuvre as the previous case ($\Omega_{avg} = 10°/s$). This results in a reduced frequency $k = \pi f c / U_\infty = 0.785$, far from the quasi-unsteady range as $k > 0.1$ thus allowing the dynamic effects on the flow with respect to the static cases. The angle of incidence along the manoeuvre is

$$\alpha = \frac{10\pi}{180} \times \left[1 - \cos\left(\frac{\pi}{2}(t - t_0)\right) \right] \quad [rad], \quad (2)$$

which gives

$$\Omega = \frac{10\pi}{180} \times \frac{\pi}{2} \sin\left(\frac{\pi}{2}(t - t_0)\right) \quad [s^{-1}]. \quad (3)$$

Figure 13 shows the sinusoidal C_L curve following a smooth hysteresis loop which matches the linear ramp case within the range of $\alpha = 0°$ and $\alpha = 20°$. The main difference between the two approaches lies in the middle part of the manoeuvre, where the sinusoidal shows a much better pitch-up performance, in exchange for a reduced C_{Lmax} and a larger lift drop at the beginning of the pitch-down phase, even reaching negative values towards the end of the cycle. Studies by Yi et al. [11] confirm this behaviour for large reduced frequencies in the unsteady range ($k > 0.1$).

Due to software limitations, it has not been possible to reproduce this non-constant pitch rate manoeuvre for the LBM approach, but the close agreement observed for the linear ramp case, seen in figure 11 has led to believe the URANS results are reliable enough for this preliminary analysis.

3.2.2 Evolution of the vortical structures

To understand the behaviour of the vortical structures over the wing when performing the manoeuvre, the position of the primary LEV is tracked. For that purpose, two positions have been analysed for the ramp manoeuvre: $x/c = 0.4$ and $x/c = 0.6$, where b is defined as the local semi-span at each location.

In figure 14, the position of the primary vortex in relation to the centre chord, measured in y/b, is depicted for the pitch-up/pitch-down manoeuvre, where y is the vortex core position in the y-axis at each section. As observed for the static case, when α increases, the vortex core moves closer to the centre chord of the delta wing, as expected. During the pitch-up manoeuvre, the trends captured with the LBM solver and the URANS solver are identical, however, the values obtained differ by around 10%. This evolution is depicted in figures 17 and 18, which illustrate the LEV development with Q-criterion iso-surfaces, where the primary vortex moves inward and
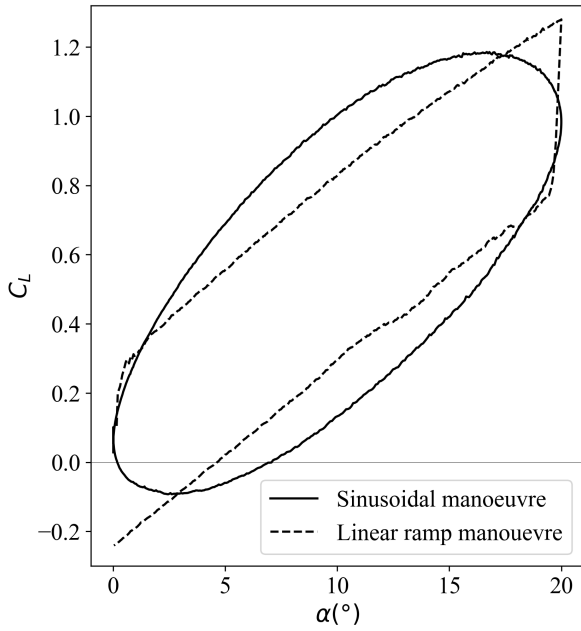
Figure 13: Lift coefficient obtained for the sinusoidal and linear ramp manoeuvres obtained with URANS

Figure 14: Evolution of the primary vortex position y/b at axial positions x/c = 0.4 (■) and 0.6 (+) for LBM (orange) and URANS (black) during pitch-up (–) and pitch-down (- -) manoeuvres.

vortex breakdown advances towards the apex through the manoeuvre.

When pitching down, the vortex core does not move closer to the leading edge, and the flow becomes substantially different from what is observed in the static case. Due to its early vortex breakdown, a consistent primary vortex is only seen up to $x/c = 0.5$, reason why the position of the vortex core is only plotted for $x/c = 0.4$. In this case, the differences between the two solvers become clear. For the URANS solver, the primary vortex position in figure 14 is nearly constant, as for the LBM solver, the primary vortex moves closer to the symmetry plane of the wing, showing a difference in spanwise position ranging
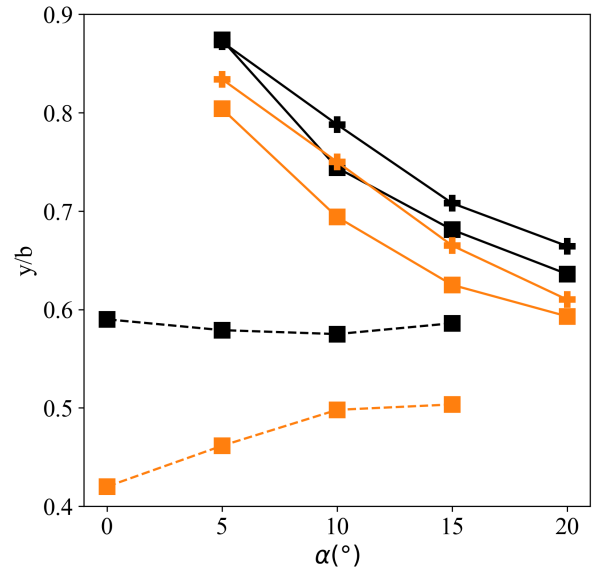
from 20% to 40% between both solvers.

In addition, as seen in figure 17, vortex breakdown advances to the apex as the wing is pitching down. This highly unsteady phenomenon is not seen as intensively for URANS as for the DNS solver, clearly observed when comparing the vortex development in figures 17 and 18.

The height of the primary vortex in relation to the wing's surface is also tracked and analysed, and its evolution is depicted in figure 16. Contrary to what was observed for its y-position, the overall trend captured for both solvers is in good agreement. For the pitch-up phase, the primary vortex moves away from the wing surface as its dimension increases with the higher incidence. As it
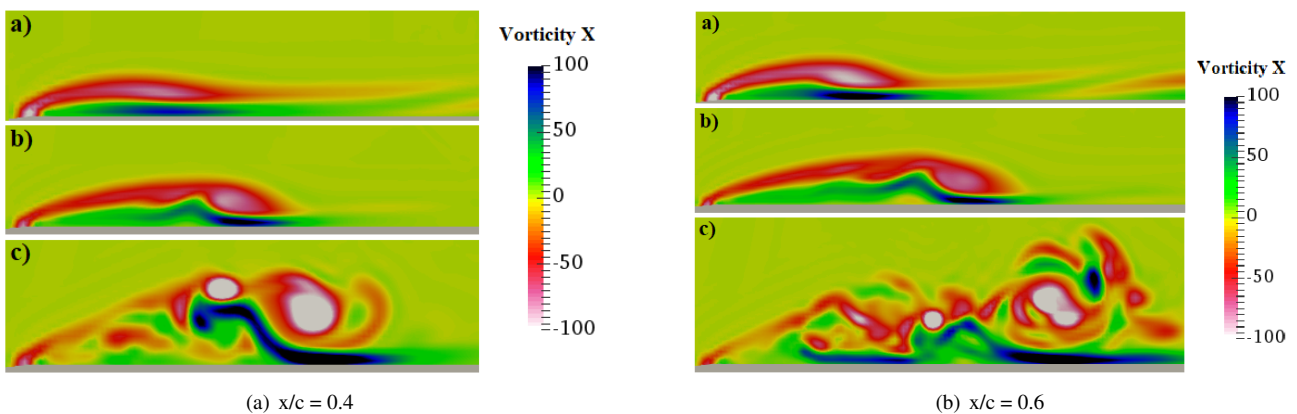

(a) x/c = 0.4

(b) x/c = 0.6

Figure 12: Streamwise vorticity obtained with LBM at two axial positions x/c for $\alpha = 5°$ at **a)** - pitch-up, **b)** - static and **c)** - pitch-down
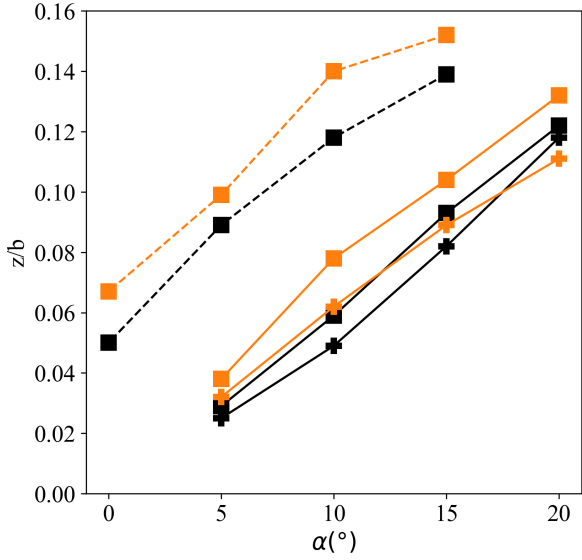
Figure 16: Evolution of the primary vortex height, z/b, at axial positions x/c = 0.4 (■), 0.6 (+) for both LBM (orange symbols) and URANS (black symbols) during pitch-up (–) and pitch-down (- -) manoeuvres.

starts to pitch down, the initial height at maximum incidence is conserved and it moves closer to the surface as the angle of attack decreases.

It is evident that the LBM solver is able to resolve the unsteady features of vortex breakdown, characteristic of the pitch-down phase of the delta wing, as opposed to the URANS solver. However, an excellent level of agreement is seen for the evolution of the lift coefficient, which provides confidence for further analyses using purely the URANS approach.

In order to further understand how the vortical structures evolve along the manoeuvre, the streamwise vorticity has been analysed and compared with the static data at $x/c = 0.4$ and $x/c = 0.6$, for $\alpha = 5°$ and $\alpha = 15°$.
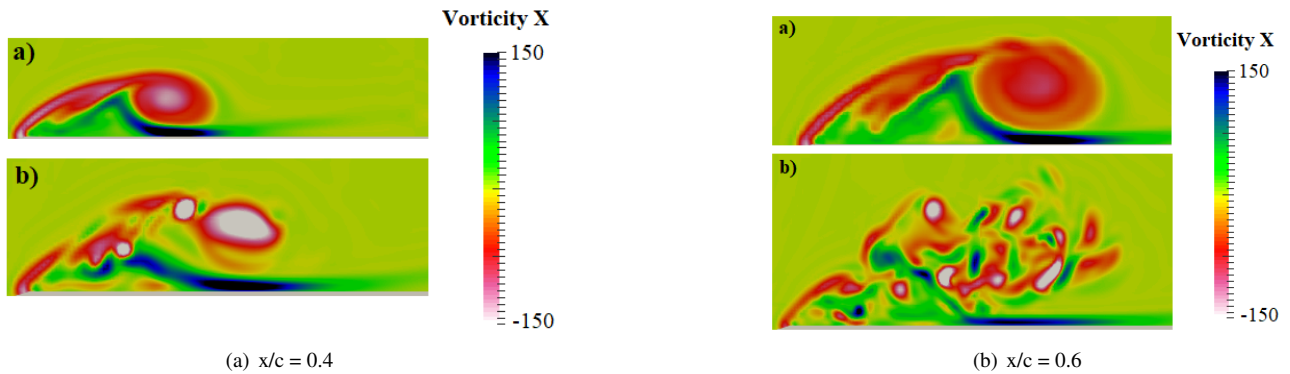
At $\alpha = 5°$, a thin shear layer can be seen at $x/c = 0.4$ when pitching up as the primary leading-edge vortex is being formed, as seen in figure 15. At $x/c = 0.6$ the primary vortex starts to be clearer. During pitch-up, a delay between the static and dynamic case is observed. This causes the LEV to adhere to the suction surface of the wing until higher angles of attack, providing higher lift overshoot, confirmed experimentally by Yi et al. [9].

For that reason, a dual vortex structure is not seen at $\alpha = 5°$ when pitching up, compared with the static case. A small weaker vortex appears inward of the primary one for the LBM solver, seen in figure 17 for $\alpha = 5°$, which is rapidly dissipated.

During the pitch-down phase, a triple vortex structure is seen at $\alpha = 5°$ at $x/c = 0.4$. This type of structure, although closer to the leading edge of the wing, is typically spotted at higher static angles of attack. This suggests that there is also a delay in the recovery of the vortical structures when pitching down. At $x/c = 0.6$, vortex breakdown has occurred and the coherent vortical structure is no longer retrieved downstream.

At $\alpha = 15°$, depicted in figure 15, the same trend is observed. When pitching up, the vortical system starts to resemble a triple vortex structure described by Raymond et al. [2], with lower intensity. Once again, this suggests that there is a time delay in the formation of the LEV due to the manoeuvre. During the pitch-down phase, as seen in figure 17, vortex breakdown moves very close to the apex of the wing. For that reason, a loss of coherence of the LEV downstream is expected, which can be confirmed in figure 15. At $x/c = 0.4$, three co-rotating vortex cores can be identified, which are rapidly dissipated as seen at $x/c = 0.6$.

(a) x/c = 0.4

(b) x/c = 0.6

Figure 15: Streamwise vorticity obtained with LBM at two axial positions x/c for $\alpha = 15°$ at **a)** - pitch-up and **b)** - pitch-down

4. CONCLUSION

The vortical flow over a $50°$ sweep delta wing with sharp leading edge was simulated with an unsteady RANS solver in *STAR-CCM+* and a DNS approach with a low-dispersion LBM. Static simulations at Re=50 000 and different angles of attack showed very close agreement between both methods in terms of force calculation, but the less computationally expensive URANS solver presented limitations when attempting to capture highly unsteady phenomena like the vortex breakdown, especially at low angles of attack due to the lower size of the unsteady flow structures.

Dynamic simulations for a $0°$-$20°$ linear pitch-up/pitch-down manoeuvre were performed with both solvers at a constant pitch rate $\Omega = \pm 10 \ °/s$. Again, an excellent agreement was observed between the lift curves corresponding to the two approaches, where these were found to follow a similar trend as the static one but with a fixed C_L translation. A time lag was observed in the development of the flow structures, where the vortex breakdown was delayed during pitch-up, effectively increasing the maximum lift coefficient and its corresponding angle of attack. During the pitch-down phase, the vortex breakdown became more intense and advanced towards the apex, resulting in a lift drop and a lower performance of the URANS solver when measuring the vortex position along the manoeuvre. A sinusoidal approach to the pitching manoeuvre, with a reduced frequency $k = 0.785$, was tested with the URANS solver and compared with the linear ramp, resulting in a C_L curve following a smoother hysteresis loop which eased simulation convergence and improved manoeuvring performance during most of the pitch-up motion.

REFERENCES

[1] PB. Earnshaw and JA. Lawford. Low-speed wind-tunnel experiments on a series of sharp-edged delta wings. *ARC Reports and Memoranda*, 3424, 1964.

[2] Raymond E. Gordnier and Miguel R. Visbal. Compact difference scheme applied to simulation of low-sweep delta wing flow. *AIAA*, 43 (8):1744–1752, 2005.

[3] E. R. Gowree, C. Jagadeesh, E. Talboys, C. Lagemann, and C. Brücker. Vortices enable the complex aerobatics of peregrine falcons. *Communications Biology*, 2018.

[4] I. Gursul, R. Gordnier, and M. Visbal. Unsteady aerodynamics of nonslender delta wings. *Progress in Aerospace Sciences*, 41 (7):515–557, 2005.

[5] J. Latt, O. Malaspinas, D. Kontaxakis, A. Parmigiani, D. Lagrava, F., M. B. Belgacem, Y. Thorimbert, S. Leclaire, S. Li, F. Marson, J. Lemus, C. Kotsalos, R. Conradin, C. Coreixas, R. Petkantchin, F. Raynaud, J. Beny, and B. Chopard. Palabos: Parallel lattice boltzmann solver. *Computers Mathematics with Applications*, 81:334–350, 2021.

[6] RE. Muir, A. Arredondo-Galeana, and IM. Viola. The leading-edge vortex of swift wing-shaped delta wings. *Royal Society Open Science*, 4 (8), 2017.

[7] EC. Polhamus. Predictions of vortex-lift characteristics by a leading-edge suction analogy. *J Aircr*, 8 (4), 1971.

[8] O. Selim, E. R. Gowree, C. Lagemann, C. Jagadeesh E. Talboys, and C. Brücker. The peregrine falcon's dive: On the pull-out maneuver and flight control through wing-morphing. *IAA Journal*, 59 (10):3979–3987, 2021.

[9] GS. Taylor, A. Kroker, and I. Gursul. Passive flow control over flexible nonslender delta wings. *AIAA*, 43, 2005.

[10] M.M. Yavuz. Transformation of flow structure on a delta wing of moderate sweep angle during pitch-up maneuver. *J. Fluids Struct.*, 33:59–69, 2012.

[11] Y. Yi, T. Hu, P. Liu, Q. Qu, G. Eitelberg, and R. Akkermans. Dynamic lift characteristics of nonslender delta wing in large-amplitude-pitching. *Aerospace Science and Technology*, 105, 2020.
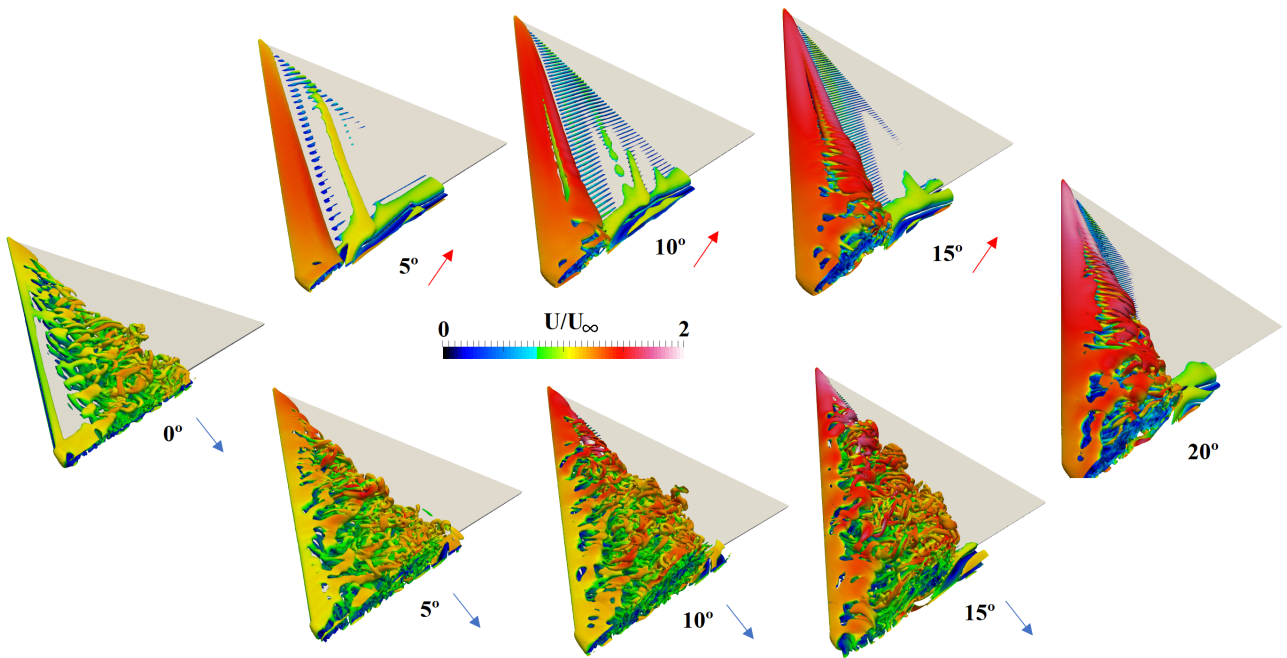
Figure 17: LEV development over the delta wing shown by Q-criterion iso-surfaces coloured by the velocity magnitude obtained for the LBM solver. The arrows indicate whether the delta wing is pitching up or down.
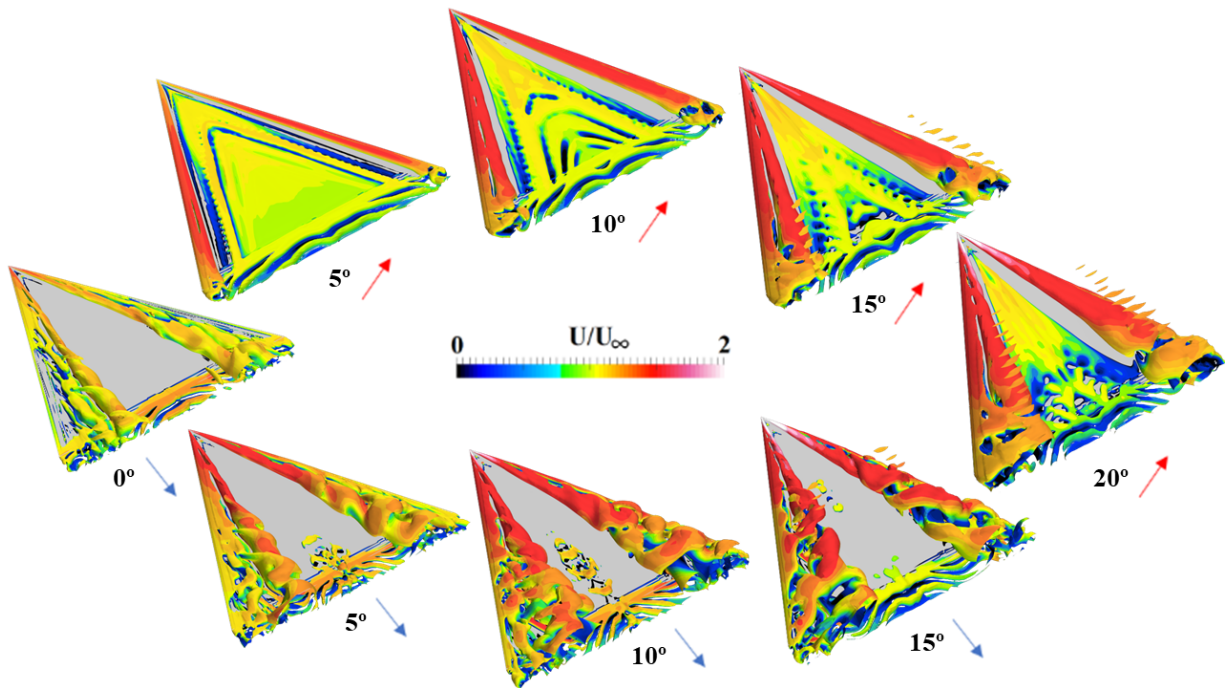

Figure 18: LEV development over the delta wing shown by Q-criterion iso-surfaces coloured by the velocity magnitude obtained in *STAR-CCM+*. The arrows indicate whether the delta wing is pitching up or down.